Spectroscopy and efficient laser operation of cleaving Yb:KY(MoO 4) 2 crystal

Anna Volokitina, Pavel Loiko, Anatoly Pavlyuk, Josep Maria Serres, Sami Slimi, Ezzedine Ben Salem, Esrom Kifle, Uwe Griebner, Valentin Petrov, Li Wang, et al.

▶ To cite this version:

Anna Volokitina, Pavel Loiko, Anatoly Pavlyuk, Josep Maria Serres, Sami Slimi, et al.. Spectroscopy and efficient laser operation of cleaving Yb:KY(MoO 4) 2 crystal. Optical Materials Express, 2020, 10 (10), pp.2356. 10.1364/OME.400894 . hal-03346000

HAL Id: hal-03346000
https://hal.science/hal-03346000

Submitted on 7 Oct 2021

Spectroscopy and efficient laser operation of cleaving Yb:KY(MoO$_4$)$_2$ crystal

ANNA VOLOKITINA,[1,2] PAVEL LOIKO,[3] ANATOLY PAVLYUK,[4] JOSEP MARIA SERRES,[1] SAMI SLIMI,[1,5] EZZEDINE BEN SALEM,[5] ESROM KIFLE,[1] UWE GRIEBNER,[6] VALENTIN PETROV,[6] LI WANG,[6] WEIDONG CHEN,[6,7] ROSA MARIA SOLÉ,[1] MAGDALENA AGUILÓ,[1] FRANCESC DÍAZ,[1] AND XAVIER MATEOS[1,*]

[1]*Universitat Rovira i Virgili (URV), Física i Cristal·lografia de Materials i Nanomaterials (FiCMA-FiCNA)-EMaS, Marcel.li Domingo 1, 43007 Tarragona, Spain*
[2]*ITMO University, 49 Kronverkskiy Pr., 197101 St. Petersburg, Russia*
[3]*Centre de Recherche sur les Ions, les Matériaux et la Photonique (CIMAP), UMR 6252 CEA-CNRS-ENSICAEN, Université de Caen Normandie, 6 Boulevard du Maréchal Juin, 14050 Caen Cedex 4, France*
[4]*A. V. Nikolaev Institute of Inorganic Chemistry, Siberian Branch of Russian Academy of Sciences, 3 Lavrentyev Ave., 630090 Novosibirsk, Russia*
[5]*I.P.E.I. of Monastir, Unit of Materials and Organic Synthesis,UR17ES31, 5019 Monastir, Tunisia*
[6]*Max Born Institute for Nonlinear Optics and Short Pulse Spectroscopy, Max-Born-Str. 2a, 12489 Berlin, Germany*
[7]*Key Laboratory of Optoelectronic Materials Chemistry and Physics, Fujian Institute of Research on the Structure of Matter, Chinese Academy of Sciences, Fuzhou, 350002 Fujian, China*
**xavier.mateos@urv.cat*

Abstract: We report on the first laser operation of ytterbium-doped potassium yttrium double molybdate crystal (Yb:KY(MoO$_4$)$_2$). Single-crystals containing 3 at.% Yb^{3+}-ions were grown by the low temperature gradient Czochralski method. The crystal structure (orthorhombic, sp. gr. D^{14}_{2h} – *Pbna*) was refined with the Rietveld method. Yb:KY(MoO$_4$)$_2$ exhibits a layered structure leading to a strong optical anisotropy and a perfect cleavage along the crystallographic (100) plane. The maximum stimulated-emission cross-section amounts to 3.70×10^{-20} cm^2 at 1008.0 nm with an emission bandwidth of 37 nm (for light polarization $\boldsymbol{E} \parallel \boldsymbol{b}$). The Stark splitting is determined at 6 K. Continuous-wave laser operation is achieved in a thin Yb:KY(MoO$_4$)$_2$ crystal plate (thickness: 286 μm) under diode pumping. The microchip laser generated a maximum output power of 0.81 W at 1021-1044 nm with a slope efficiency of 76.4% and polarized emission. Yb:KY(MoO$_4$)$_2$ crystal lamellae / plates are attractive for sub-ns passively Q-switched microchip lasers and thin-disk lasers.

1. Introduction

Cleavage is the property of crystalline materials to split along certain crystallographic planes. The simplest case is basal or pinacoidal cleavage when this happens along only a single plane. It may result from a weaker bond strength or larger lattice spacing perpendicular to the plane, and it is frequently observed in crystals with a regular location of atoms forming “layers”. As a result, crystalline plates with continuous, smooth and flat faces, both strictly parallel to the so-called cleavage plane are easily obtained. An example of a cleaving mineral is mica showing perfect (or even “eminent”) cleavage. Crystals with perfect cleavage can cleave without leaving any rough surface (mirror-quality) [1]. Cleavage is used for identification of minerals. It is also useful for chipping of wafers of semiconductor crystals (e.g., silicon).

Laser crystals exhibiting perfect cleavage along a crystallographic plane are known [1-3]. On the one hand, this complicates their mechanical processing (cutting and polishing). On the other hand, it can turn out to be a useful feature for applications where thin laser elements with a large aperture and good parallelism / optical quality of the faces are required. Moreover, this simplifies fabrication of laser elements, especially for soft crystals. Two examples are the microchip and thin-disk lasers. In particular, a microchip laser consists of a thin (typically, few hundred μm thick) gain medium placed in a simple plano-plano cavity without air gaps, leading to a highly-compact and monolithic design (optionally, one or both of the cavity mirrors are coated on the crystal faces) [4]. Note a positive thermal lens of the gain material for stabilizing the laser mode of microchip lasers is an important requirement [5]. This robust design is almost insensitive to misalignment and leads to low intracavity losses, low laser threshold, good cavity stability and very short cavity roundtrip time beneficial for achieving sub-ns pulses in passively Q-switched lasers [6].

So far, only few crystals doped with rare-earth ions (RE^{3+}) such as Nd^{3+}, Yb^{3+} or Tm^{3+} showing perfect cleavage have been applied for lasers in the near-IR, cf. Table 1. These include borates (LaB_3O_6) [7], phosphates (YPO_4 and $LuPO_4$) [8,9] and molybdates ($BaGd_2(MoO_4)_4$) [10]. Other cleaving crystals were proposed as potential laser materials (e.g., $CsGd(MoO_4)_2$) [11] but no laser operation has been reported so far. Yb^{3+}-doped materials are known for efficient laser operation at ~1 μm on the $^2F_{5/2} \rightarrow {}^2F_{7/2}$ electronic transition. The Yb^{3+} ion can be easily pumped by commercially available high-power InGaAs laser diodes emitting at ~0.96-0.98 μm [12]. It also exhibits a simple energy level scheme eliminating parasitic energy-transfer processes. In-band pumping of Yb^{3+} leads to high pump Stokes efficiency, and, thus, reduced heat load and slope efficiencies up to ~80% [13]. Moreover, as compared to Nd^{3+}, Yb^{3+} shows larger Stark splitting of the ground-state ($^2F_{7/2}$) and, consequently, broader emission at ~1 μm, beneficial for broadly tunable and mode-locked lasers. Liu *et al.* reported on a diode-pumped $Yb:LuPO_4$ laser based on a (100)-oriented unprocessed as-grown crystal plate delivering 1.61 W at 1036-1040 nm with a slope efficiency of 75% [8]. Zhu *et al.* used cleaved plates of $Yb:BaGd_2(MoO_4)_4$ and produced a similar output power (1.16 W at 1046-1054 nm) albeit with much lower slope efficiency (20%) [1].

Table 1. Laser Performance^a of RE^{3+}-doped Cleaving Crystals

Crystal	Plane	t, mm	P_{out}, W	λ_L, nm	η, %	P_{th}, W	Ref.
$Nd:LaB_3O_6$	(101)	0.5	0.53	1060	49	~0.03	[7]
$Nd:YPO_4$	(010)	0.6	2.16	1063	56.4	0.22	[9]
$Nd:BaGd_2(MoO_4)_4$	(010)	1.1	0.70	1061	51	<0.01	[14]
$Yb:LuPO_4$	(100)	0.3	**1.61**	1036-1040	75	0.17	[8]
$Yb:BaGd_2(MoO_4)_4$	(010)	4.0	1.16	1046-1054	20	5.8	[1]
$Yb:KY(MoO_4)_2$	(100)	0.29	0.81	1021-1044	**76.4**	**0.06**	This work
$Tm:KY(MoO_4)_2$	(100)	0.70	0.88	1840-1905	65.8	0.21	[3]
$Tm:BaGd_2(MoO_4)_4$	(010)	1.6	0.35	1905-1921	49	0.1	[10]

$^a t$ - thickness, P_{out} - output power, λ_L - laser wavelength, η -slope efficiency, P_{th} - laser threshold.

Among the host crystals for Yb^{3+} doping, complex tungstates and molybdates are attracting a lot of attention. Their advantages include: (i) high attainable Yb^{3+} doping concentrations; (ii) weak luminescence quenching, (iii) low non-radiative relaxations and luminescence quantum yields approaching unity, (iv) polarized, intense and broad absorption and emission bands at 1 μm, and (v) Raman activity. A prominent example is the crystal family of monoclinic double tungstates with chemical formula $KLn(WO_4)_2$, where Ln = Gd, Y or Lu [15,16]. Efficient continuous-wave [12,17], passively Q-switched [6] and especially mode-locked [18,19] $Yb:KLn(WO_4)_2$ lasers are known. Thin-disk lasers based on these materials were also demonstrated using thin bulk or epitaxial samples [20,21].

Compared to the above mentioned potassium double tungstates, their double molybdate (DMo) counterparts with chemical formula $KLn(MoO_4)_2$ have been barely studied. One example of the DMo crystal family is potassium yttrium double molybdate, $KY(MoO_4)_2$ [22-

24]. It is orthorhombic and exhibits an interesting layered structure together with a low-symmetry site for the RE ions (C_2) leading to a strong anisotropy of the optical properties as well as to the natural cleavage habit [22]. The structure and vibronic properties of undoped $KY(MoO_4)_2$ have been reported [25,26]. The RE^{3+} site symmetry was revealed using Eu^{3+} as a structural probe [22]. Very recently, we achieved laser operation in cleaved single-crystalline plates and thin films of Tm:$KY(MoO_4)_2$ [3]. A crystal-plate laser generated 0.88 W at 1840-1905 nm with a slope efficiency of 65.8%. The concept of the *thin-film* laser using cleaved Nd:$KY(MoO_4)_2$ was first proposed [27] by Kaminski *et al*.

In the present work, we demonstrate laser operation of a Yb:$KY(MoO_4)_2$ crystal, for the first time to the best of our knowledge, by using its perfect cleavage feature.

2. Crystal growth

The Yb:$KY(MoO_4)_2$ compound melts at ~1243 K. The single crystals were grown by the Low Temperature Gradient (LTG) Czochralski method [28]. As raw materials, we used Y_2O_3 (purity: 5N), Yb_2O_3 (4N), MoO_3 (4N) and K_2CO_3 (5N) taken according to the composition 95-93mol% $KY_{0.97}Yb_{0.03}(MoO_4)_2$ solute – 5-7 mol% $K_2Mo_3O_{10}$ solvent assuming substitution of Y^{3+} ions by the Yb^{3+} dopants (3 at.% Yb). The potassium trimolybdate ($K_2Mo_3O_{10}$) was added to the melt to prevent its partial dissociation resulting in the formation of yttrium oxomolybdate (Y_2MoO_6) and, thus, to stabilize the growth process [22]. The raw materials were mixed and placed in a Pt crucible. It was heated up to ~1320 K in air and kept at this temperature for 2–3 hours to homogenize the melt. Then, it was cooled to ~1240 K (the temperature where the growth started). A [100]-oriented seed from an undoped $KY(MoO_4)_2$ was used. It was rotated at 20 rpm, the pulling rate was 1–2 mm/h and the cooling rate was ~2 K/day. The temperature gradient in the melt was below 3 K/cm (in the vertical direction). After completing the growth, the crystal was removed from the melt and slowly cooled down to room temperature (RT, 293 K). No annealing was applied. More details can be found elsewhere [3,22].

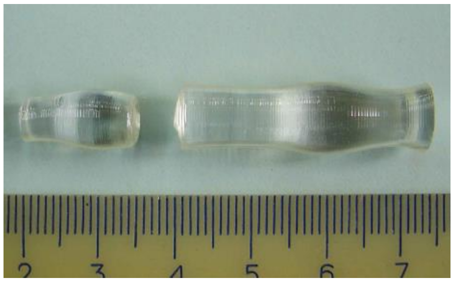

Fig. 1. A photograph of as-grown 3 at.% Yb:$KY(MoO_4)_2$ crystals. The growth direction is along the [100] crystallographic axis.

The as-grown crystals were transparent and colorless, Fig. 1. They had a cylindrical shape with an elliptic cross-section with the semiaxes oriented along the [010] and [001] directions. Neither cracks nor inclusions were observed. The crystals showed an easy cleavage along the (100) plane (orthogonal to the growth direction). The orientation of the [010] and [001] axes was determined by single-crystal X-ray diffraction.

The actual Yb^{3+} doping concentration was determined by Energy Dispersive X-ray (EDX) spectroscopy to be $N_{Yb} = 2.3 \pm 0.5 \times 10^{20}$ cm^{-3} (~3.0 at.% Yb), so that the segregation coefficient for Yb^{3+} doping $K_{Yb} = N_{crystal}/N_{melt}$ was close to unity.

3. Crystal structure

3.1 Rietveld refinement

The structure and phase purity of the 3 at.% Yb:KY(MoO_4)$_2$ was confirmed by X-ray powder diffraction (XRD), Fig. 2(a). The measurements were carried out in a θ-θ Bragg Brentano configuration using a Siemens D-5000 powder X-ray diffractometer with Cu Kα (1.5406 Å) radiation. The XRD pattern was recorded in a 2θ range from 10° to 65°, a step size of 0.02° and a step time of 16 s. The crystal belongs to the orthorhombic class (sp. gr. *Pbna* – D^{14}_{2h}, centrosymmetric point group 2/*m*). Note that we use the non-conventional space group (the standard one is *Pbcn*, No. 60), following the early publications [25,29]. The unit cell parameters refined using the Le Bail method are: a = 18.212(2) Å, b = 7.9343(6) Å, c = 5.0705(5) Å (number of the formula units in the unit-cell Z = 4). The obtained *R*-factors were R_{wp} = 6.44% and R_{exp} = 5.19% (the reduced χ-squared value $\chi^2 = (R_{\mathrm{wp}}/R_{\mathrm{exp}})^2 = 1.54$). The calculated volume of the unit cell V is 732.7(1) Å^3 and the crystal density ρ_{calc} = 4.083(6) g/cm^3. The structure from [22] was taken as the starting one for the refinement. The fractional atomic coordinates were refined by the Rietveld method using the TOPAS software, see the results in Table 2, with the fixed unit cell parameters obtained by the Le Bail's method and considering the (100) preferred orientation. For this refinement, R_{wp} = 8.90% and R_{exp} = 5.19% (χ^2 = 2.94). Figure 2 shows the Rietveld refinement plot with the observed, calculated and difference patterns. No other phases except the orthorhombic one are found in the pattern. The min / max residual electron densities are -0.6 *e*/Å^3 and +0.1 *e*/Å^3, respectively.

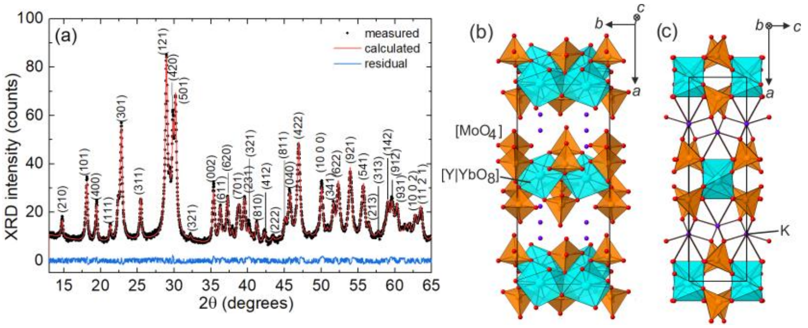

Fig. 2. (a) Rietveld analysis of the RT X-ray powder diffraction (XRD) pattern of a 3 at.% Yb:KY(MoO_4)$_2$ crystal, the numbers denote the Miller's indices (*hkl*) for the sp. gr. *Pbna*; (b,c) Illustration of the layered structure of the Yb:KY(MoO_4)$_2$ crystal: (b) three-dimensional view, (c) a projection of the ***a-c*** plane. *Black rectangle* denotes the unit-cell.

Table 2. Fractional Atomic Coordinates (*x, y, z*), Occupancy Factors (O.F.) and Temperature Factors (B_{iso}) for 3 at.% Yb:KY(MoO_4)$_2$ (Space Group *Pbna*)

Atom	Wyckoff symbol	*x*	*y*	*z*	O.F.	B_{iso}
K	4*c*	0.2713(4)	0.25	0	1	2.6(3)
Y	4*c*	0.5060(2)	0.25	0	0.97	0.94(1)
Yb	4*c*	0.5060(2)	0.25	0	0.03	0.94(1)
Mo	8*d*	0.1014(1)	-0.0163(3)	0.0204(6)	1	0.83(8)
O1	8*d*	0.1885(6)	0.531(2)	0.102(2)	1	1.6(2)
O2	8*d*	0.1001(1)	0.834(2)	0.245(2)	1	1.6(2)
O3	8*d*	0.1039(1)	0.164(2)	0.230(2)	1	1.6(2)
O4	8*d*	0.4716(7)	-0.034(4)	0.2804(2)	1	1.6(2)

The unit-cell parameters are slightly smaller than those for undoped KY(MoO_4)$_2$, a = 18.23 Å, b = 7.95 Å, c = 5.07 Å [25]. In KY(MoO_4)$_2$, the Yb^{3+} ions substitute for the Y^{3+} ones in a single type of crystallographic sites (Wyckoff symbol: 4*c*, site symmetry: C_2, coordination number (C.N.): VIII). The corresponding ionic radii are R_{Yb} = 0.985 Å and R_{Y} = 1.019 Å for VIII-fold oxygen coordination [30], explaining the observed decrease of the lattice constants. The closeness of the ionic radii of Yb^{3+} and Y^{3+}, the existence of the orthorhombic stoichiometric KYb(MoO_4)$_2$ phase [31] and the homovalent doping mechanism also explain the observed $K_{\mathrm{Yb}} \approx 1$.

Using the refined atomic coordinates, the structure of Yb:KY(MoO$_4$)$_2$ is illustrated in Fig. 2(b,c). The corresponding interatomic distances are listed in Table 3. The C.N. for Mo^{6+} cations is 4+1: a distorted tetrahedral coordination (with 4 closely located oxygens, with the Mo – O distances lying in the range 1.644(8) – 1.847(6) Å and 1 more distant oxygen at 2.5735 Å). For K$^+$, the C.N. is 6+4, defined in a similar manner. The closest 6 oxygens are at 2.742(1) - 2.759(6) Å, while the other oxygens are at 3.335(2) – 4.223(0) Å. Such a coordination behavior is common for tungstates and molybdates with a C.N. of W (or Mo) of V or VI, where the cation – anion distances may vary in a broad range, so that a formal definition of the C.N. is not possible [25]. For the distorted [Y|YbO$_8$] polyhedra (bicapped octahedra), the bond lengths are in the range 2.26(2) - 2.74(3) Å. The belts of edge-sharing [Y|YbO$_8$] polyhedra run along the ***b***-axis. Along the ***c***-axis, they are separated by an empty polyhedron which is sharing 4 edges with four [MoO$_4$] tetrahedra. Each Mo-tetrahedron connects two translationally identical belts of Y-polyhedra and, simultaneously, it connects the corners of two adjacent Y-polyhedra (within the belt). Thus, the multi-layer structure of Yb:KY(MoO$_4$)$_2$ is determined by [Y|Yb(MoO$_4$)$_2$] layers (lying in the ***b***-***c*** plane) formed by [MoO$_4$] tetrahedra and [Y|YbO$_8$] polyhedra and containing cavities, as well as zigzag K$^+$-layers separating two neighboring [Y|Yb(MoO$_4$)$_2$] layers. The zigzag K$^+$-layers are more loose than the [Y|Yb(MoO$_4$)$_2$] ones. Moreover, the latter are separated by a relatively large *a*/2 spacing of 9.106 Å. This determines the natural cleavage along the (100) plane.

Table 3. Selected Interatomic Distances in 3 at.% Yb:KY(MoO$_4$)$_2$

Distances (Å)		
[Y|Yb]O$_8$	[Mo]O$_{4+1}$	[K]O$_{6+4}$
Y|Yb – O4 = 2.261(2) ×2	Mo – O3 =1.784(6) ×1	K – O1 = 2.742(1) ×2
Y|Yb – O3 = 2.348(0) ×2	Mo – O4 = 1.847(6) ×1	K – O1' = 2.759(6) ×2
Y|Yb – O2 = 2.418(9) ×2	Mo – O2 = 1.644(8) ×1	K – O2 = 2.756(2) ×2
Y|Yb – O4' = 2.743(1) ×2	Mo – O1 = 1.708(7) ×1	K – O2' = 3.335(2)×1
Y|Yb – Y|Yb = 3.973(2) ×2[a]	Mo – O4 = 2.5735 ×1	K – O1'' = 3.587(6) ×2
Y|Yb – Y|Yb = 5.071(5) ×2[b]		K – O3 = 4.223(0) × 1

[a,b] The shortest Y|Yb – Y|Yb distances are added for comparison. [a] Along the ***b***-axis. [b] Along the ***c***-axis (sp. gr. *Pbna*).

The shortest Y|Yb – Y|Yb distance is 3.973 Å (along the ***b***-axis, in the layer plane). It is relatively long and similar to that (Y – Y) in the monoclinic KY(WO$_4$)$_2$ crystal (4.06 Å) [22]. This distance determines the weak cross-talk of Yb^{3+} ions (weak concentration quenching of luminescence) along the ***a***-axis (orthogonal to the layer plane), 9.45 Å.

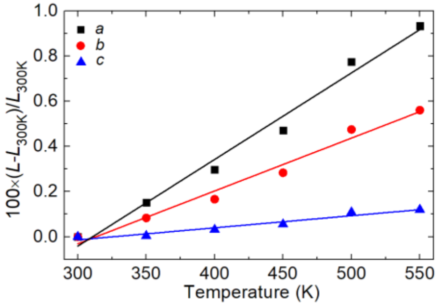

Fig. 3. Relative thermal evolution of the unit cell parameters of 3 at.% Yb:KY(MoO$_4$)$_2$ with the temperature up to 550 K.

The coefficients of thermal expansion (CTE) of Yb:KY(MoO$_4$)$_2$ were calculated from the temperature dependence of the lattice constants determined by high-temperature powder XRD. For the XRD studies in the temperature range of 300–550 K, we used a temperature chamber (HTK10). The heating rate was 0.17 K/s with a delay of 300 s before each measurement. The 2θ angle varied from 10º to 70º with a step size of 0.03º and a step time of 5 s. The relative evolution of the unit cell parameters with temperature is shown in Fig. 3. The linear thermal expansion tensor (α_{ij}) in *abc* frame was obtained from the slopes of the linear fits shown in Fig. 3. Thus, (α_{ij}) is:

$$(\alpha_{\mathrm{ij}}) = \begin{pmatrix} 38.3 & 0 & 0 \\ 0 & 23.4 & 0 \\ 0 & 0 & 5.36 \end{pmatrix} \times 10^{-6}\,\mathrm{K}^{-1}. \tag{1}$$

The coefficient of the volumetric thermal expansion, $\alpha_{\mathrm{vol}} = \alpha_{\mathrm{a}} + \alpha_{\mathrm{b}} + \alpha_{\mathrm{c}}$ is 67.1×10^{-6} K^{-1}.

The anisotropy of the thermal expansion in Yb:KY(MoO_4)$_2$ is relatively strong, as expressed by the ratios $\alpha_{\mathrm{a}} : \alpha_{\mathrm{b}} = 1.64$ and $\alpha_{\mathrm{a}} : \alpha_{\mathrm{c}} = 7.15$. The thermal expansion in KY(MoO_4)$_2$ is stronger than in its double tungstate counterpart. Indeed, for KY(WO_4)$_2$, $\alpha_{\mathrm{a}} = 8.4$, $\alpha_{\mathrm{b}} = 2.0$ and $\alpha_{\mathrm{c*}} = 19.8$ [10^{-6} K^{-1}] [32].

The thermal conductivity of KY(MoO_4)$_2$ is unknown but it is expected to be higher in the layer plane.

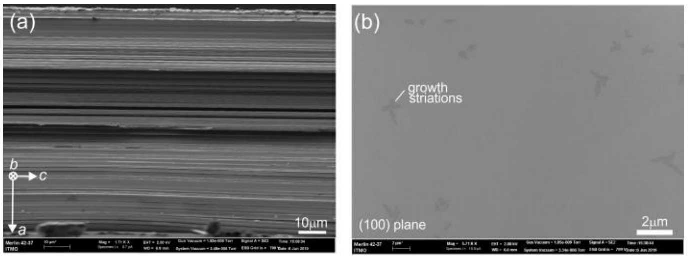

Fig. 4. Scanning Electron Microscope (SEM) images of a cleaved single-crystal plate of 3 at.% Yb:KY(MoO_4)$_2$: (a) the fracture edge of the plate running along the ***c***-axis, the ***a***-axis is vertical; (b) the plate surface parallel to the (100) plane showing flower-like defects.

By mechanical cleavage orthogonal to the crystal growth direction (along the (100) plane), we produced single-crystalline plates of Yb:KY(MoO_4)$_2$ with a thickness (t) as thin as 100 μm. They were studied by Scanning Electron Microscopy (SEM) using a MERLIN microscope (Carl Zeiss). Under bending, the plates exhibited an elastic deformation along the [010] axis and broke with the fracture edge running parallel to the [001] axis, Fig. 4(a). This SEM image shows multiple “steps” parallel to the (100) cleavage plane. Both surfaces of the cleaved plates had mirror-quality. No polishing was applied to them. The SEM study in the μm-scale revealed dark flower-like defects, Fig. 4(b); however, the concentration of these defects was low. The clean aperture of the obtained crystal-plates was >1 cm^2. They contained no macroscopic cracks.

3.2 Raman spectra

Molybdate crystals are known as efficient Raman-active materials. Thus, Yb:KY(MoO_4)$_2$ can serve for self-frequency Raman conversion. The RT polarized Raman spectra were measured using a confocal Raman microscope (Renishaw inVia) equipped with an ×50 objective, an edge filter and an Ar$^+$ ion laser (488 nm). A cleaved crystal plate (***a***-cut) was used and the excitation / collection geometries were ***a***(*mn*)***a***, where *m*, *n* = ***b***, ***c*** (according to Porto’s notations).

The Raman spectra are shown in Fig. 5. They are strongly polarized with the most intense Raman response in the ***a***(***bb***)***a*** geometry. The observed bands are classified into three groups of vibrations [22,26]. The low-frequency range, 80-272 cm^{-1}, contains translational (T') and rotational (R') modes of the K, Y|Yb and Mo cations. Internal bending vibrations (δ) of the oxygen bridged [MoO_4] tetrahedra are observed in the intermediate frequency range, 315–435 cm^{-1}. The high-frequency range, 726-944 cm^{-1}, contains intense stretching vibrations (ν) of these tetrahedra. The gap in the Raman spectra (500-700 cm^{-1}) is due to the relatively weak oxygen linkage of the [MoO_4] tetrahedra in the layer plane. This feature is similar to the one found in scheelite ($CaWO_4$) type double tungstate and molybdate crystals with isolated [WO_4] tetrahedra [33].

The most intense Raman mode is at 865 cm^{-1} with a width at half maximum (FWHM) of 18.8 cm^{-1}. The maximum phonon energy $h\nu_{max}$ is 944 cm^{-1}.

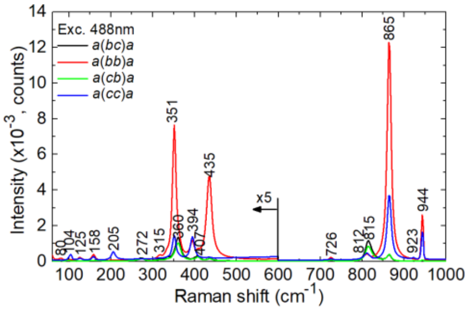

Fig. 5. RT Raman spectra of the 3 at.% Yb:KY(MoO_4)$_2$ crystal for the ***a***(*mn*)***a***, *m*, *n* = ***b***, ***c*** geometries (Porto's notations), λ_{exc} = 488 nm, *numbers* indicate the peak frequencies in cm^{-1}.

4. Optical spectroscopy

4.1 Optical absorption

Orthorhombic KY(MoO_4)$_2$ is an optically biaxial crystal. Only a mean value of its refractive index is known, $\langle n \rangle \approx 1.95$. KY($MoO_4$)$_2$ shows a strong birefringence, Δn = 0.018 – 0.087 [34]. The optical indicatrix axes coincide with the crystallographic axes. We will denote the principal light polarizations as ***E*** || ***a***, ***b*** and ***c***.

The absorption spectra were measured using a Varian CARY-5000 spectrophotometer (0.3-2 μm) and a FTIR spectrometer Bruker Tensor 27 (2-7 μm). A Glan-Taylor prism was used for polarization-resolved studies.

The transmission spectrum of a ~1 cm-thick 3 at.% Yb:KY(MoO_4)$_2$ crystal sample is shown in Fig. 6(a) revealing a transparency range from 0.33 to 3.4 μm (extending up to 5 μm to some extent). The structured absorption at longer wavelengths is related to the ν vibrations of the MoO_4 tetrahedra. The infrared cut-off is due to the $2\nu_1$ overtone peak of the $[MoO_4]^{2-}$ group fundamental vibration.

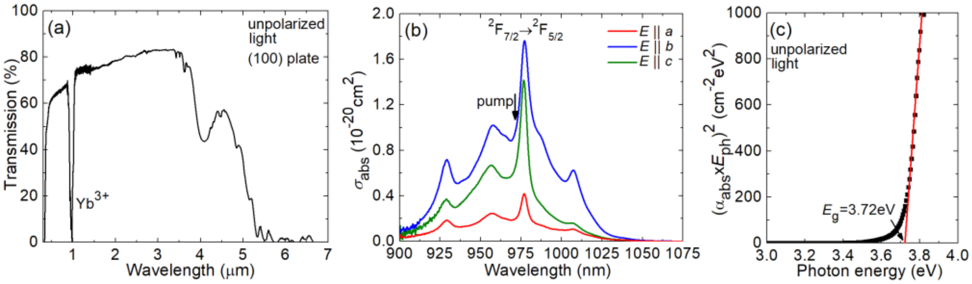

Fig. 6. RT absorption properties of a 3 at.% Yb:KY(MoO_4)$_2$ crystal: (a) unpolarized transmission spectrum of a ~1 cm-thick (100)-oriented crystal plate; (b) absorption cross-section, σ_{abs}, spectra for light polarizations ***E*** || ***a***, ***b***, ***c***. The *arrow* indicates the pump wavelength used in the laser experiments; (c) Tauc plot for the evaluation of the optical bandgap (E_g), E_{ph} – photon energy.

The absorption at ~1 μm originates from the $^2F_{7/2} \rightarrow {}^2F_{5/2}$ transition of Yb^{3+} ions. It is analyzed in Fig. 6(b) in terms of absorption cross-sections, $\sigma_{abs} = \alpha_{abs}/N_{Yb}$ (α_{abs} - absorption coefficient) for the principal light polarizations ***E*** || ***a***, ***b***, ***c***. The absorption spectra exhibit strong polarization anisotropy. The maximum σ_{abs} is 1.77×10^{-20} cm^2 at 977.1 nm and the

FWHM of the absorption peak is 19.6 nm for light polarization ***E*** || ***b***. This wavelength corresponds to the zero-phonon line (ZPL, see below) transition at RT. For the other two light polarizations, the absorption cross-sections are lower, as expressed by the ratios $\sigma_{\mathrm{abs}}(\boldsymbol{b})$: $\sigma_{\mathrm{abs}}(\boldsymbol{c})$ = 1.26 and $\sigma_{\mathrm{abs}}(\boldsymbol{b})$: $\sigma_{\mathrm{abs}}(\boldsymbol{a})$ = 4.2 at ~980 nm. This anisotropy arises, in part, from the layered crystal structure (note the significant drop of the optical absorption for light polarized orthogonal to the ***b***-***c*** layer plane) and, in part, from the low symmetry of the Yb^{3+} site. The observed broad absorption spectra qualify Yb:KY$(\mathrm{MoO}_4)_2$ for diode-pumping by InGaAs laser diodes emitting at ~980 nm.

The absorption cross-sections in Yb:KY$(\mathrm{MoO}_4)_2$ are lower than those for the monoclinic Yb:KY$(\mathrm{WO}_4)_2$ crystal: $\sigma_{\mathrm{abs}} = 10.8\times10^{-20}$ cm^2 at 981.0 nm corresponding a narrower FWHM of 4.0 nm (for light polarization ***E*** || N_{m}) [35].

The optical bandgap of Yb:KY$(\mathrm{MoO}_4)_2$ was evaluated with the Tauc plot, i.e, by plotting $(\alpha_{\mathrm{abs}}\times E_{\mathrm{ph}})^2$ *vs*. the photon energy $E_{\mathrm{ph}} = h(c/\lambda)$. The intersection of the linear fit of the obtained plot with the horizontal axis yields E_{g} = 3.72 eV (the wavelength of the UV absorption edge is ~330 nm).

4.2 Luminescence: spectra and lifetime

The polarized luminescence spectra were measured using an optical spectrum analyzer (OSA, Hamamatsu, AQ6373) and a Glan-Taylor polarizer. The stimulated-emission (SE) cross-sections, σ_{SE}, for *i*-th polarization (*i* = ***a***, ***b***, ***c***) were calculated from the measured luminescence spectra calibrated for the spectral response of the set-up $W'(\lambda)$ using the Füchtbauer–Ladenburg (F-L) formula [36]:

$$\sigma_{\mathrm{SE}}^{i}(\lambda) = \frac{\lambda^5}{8\pi\langle n\rangle^2\tau_{\mathrm{rad}}c}\frac{3W'_i(\lambda)}{\sum\limits_{i=a,b,c}\int\lambda W'_i(\lambda)\mathrm{d}\lambda}, \qquad (2)$$

where λ is the wavelength, $<n> \approx 1.95$ is the refractive index, *c* is the speed of light in vacuum and τ_{rad} = 458 μs is the radiative lifetime of the emitting level ($^2\mathrm{F}_{5/2}$), see below. The results are shown in Fig. 7(a).

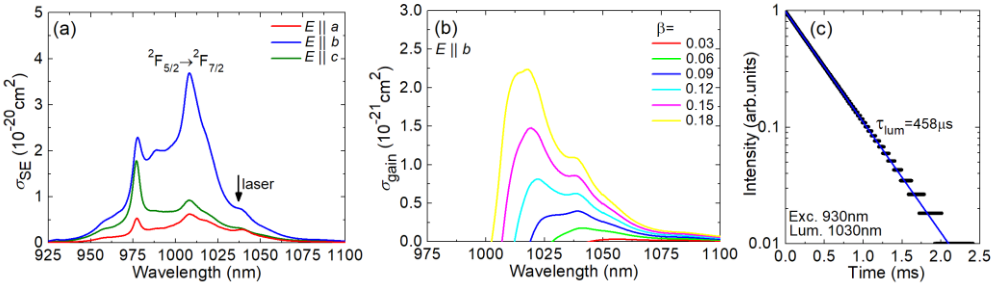

Fig. 7. Emission properties of Yb^{3+}:KY$(\mathrm{MoO}_4)_2$: (a) stimulated-emission (SE) cross-sections, σ_{SE}, for light polarizations ***E*** || ***a***, ***b*** and ***c***. The *arrow* indicates the observed laser wavelength; (b) gain cross-sections, $\sigma_{\mathrm{gain}} = \beta\sigma_{\mathrm{SE}} - (1-\beta)\sigma_{\mathrm{abs}}$, $\beta = N_2(^2\mathrm{F}_{5/2})/N_{\mathrm{Yb}}$ is the inversion ratio, the light polarization is ***E*** || ***b***; (c) luminescence decay curve for a cleaved film, λ_{exc} = 930 nm, λ_{lum} = 1030 nm, *symbols*: experimental data, *line*: single-exponential fit.

For Yb:KY$(\mathrm{MoO}_4)_2$, the maximum σ_{SE} amounts to 3.70×10^{-20} cm^2 at 1008.0 nm and the emission bandwidth (FWHM) $\Delta\lambda_{\mathrm{em}}$ is 37.0 nm for the high-gain light polarization ***E*** || ***b***. The emission spectra are also strongly polarized, as expressed by the ratios $\sigma_{\mathrm{SE}}(\boldsymbol{b})$: $\sigma_{\mathrm{SE}}(\boldsymbol{c})$ = 3.9 and $\sigma_{\mathrm{SE}}(\boldsymbol{b})$: $\sigma_{\mathrm{SE}}(\boldsymbol{a})$ = 6.0 at ~1.01 μm. These high ratios are a prerequisite for linearly polarized laser emission. Note that (100)-oriented crystal plates give access to the preferable light polarization ***E*** || ***b***. Compared to its monoclinic double tungstate counterpart, Yb:KY$(\mathrm{WO}_4)_2$, for which $\sigma_{\mathrm{SE}} = 3.2\times10^{-20}$ cm^2 at 1021.9 nm with $\Delta\lambda_{\mathrm{em}}$ = 30.2 nm for ***E*** || N_{m} [35], Yb:KY$(\mathrm{MoO}_4)_2$ provides higher SE cross-sections and broader emission bandwidth. These are attractive features for broadly tunable and ultrashort-pulse lasers at ~1 μm.

For the Yb^{3+} ion, exhibiting reabsorption at the laser wavelength, the spectral behavior of the laser depends on the output-coupling losses via the rate of inversion in the gain medium, expressed by the inversion ratio $\beta = N_2(^2F_{5/2})/N_{Yb}$, where N_2 is the population of the upper level ($^2F_{5/2}$) and $N_1 + N_2 = N_{Yb}$. Thus, the gain cross-sections, $\sigma_{gain} = \beta\sigma_{SE} - (1 - \beta)\sigma_{abs}$, are calculated to predict the possible laser wavelengths for different β. The gain spectra for light polarization $\boldsymbol{E} \parallel \boldsymbol{b}$ are shown in Fig. 7(b). For small $\beta < 0.03$, the gain spectra are very flat and broad extending from ~1040 nm to 1100nm. For intermediate inversion ratios $0.05 < \beta < 0.10$, a local peak in the spectra appears at ~1039 nm. For even higher inversion ratios, another maximum at a shorter wavelength of ~1019 nm is observed. For $\beta = 0.15$, the gain bandwidth $\Delta\lambda_g$ is 33.0 nm in agreement with the luminescence studies.

The luminescence decay curve of the sample was measured using an InGaAs photodetector under ns pulse excitation from an optical parametric oscillator (Horizon, Continuum) tuned to 930 nm, a 1/4 m monochromator (Oriel 77200) and an 8 GHz oscilloscope (DSA70804B, Tektronix). A thin (~30 μm) cleaved film was used to avoid the effect of radiation trapping. The decay curve plotted in a semi-log scale, Fig. 7(c), is single-exponential in agreement with a single type of Yb^{3+} sites. The luminescence decay time τ_{lum} = 458 μs is longer than that of monoclinic Yb:KY$(WO_4)_2$ crystals (τ_{lum} = 231 μs [35]).

4.3 Crystal-field splitting

For Yb^{3+} ions in C_2 sites, each $^{2S+1}L_J$ multiplet is split into $J + 1/2$ Stark sub-levels which are numbered as 0...3 for the ground-state ($^2F_{7/2}$) and 0'...2' for the excited-state ($^2F_{5/2}$). To resolve their energies, we measured the unpolarized absorption and luminescence spectra at low temperature (LT, 6 K) using an Oxford Instruments Ltd. cryostat (model SU 12) with helium-gas close-cycle flow. The results are shown in Fig. 8. The LT spectra were interpreted accounting for the Raman spectra in order to assign the possible vibronic sidebands.

The zero-phonon line (ZPL) is the transition between the lowest Stark sub-levels of both multiplets, designated as 0 ↔ 0'. It is observed at 10246 cm^{-1} corresponding to the wavelength of 976.0 nm (at 6 K). The full set of energy-levels of Yb^{3+}:KY$(MoO_4)_2$ is $^2F_{7/2}$ = (0, 315, 411, 601) cm^{-1} and $^2F_{5/2}$ = (10246, 10440, 10749) cm^{-1}, see Fig. 9(a), showing the energy-level scheme and the wavelengths of the electronic transitions in absorption and emission. In particular, the emission peak at ~1007 nm corresponding to the maximum SE cross-sections is assigned to the 0' → 1 transition. The partition functions for the lower (m = 1) and upper (m = 2) manifolds are Z_1 = 1.397 and Z_2 = 1.469 (the ratio Z_1/Z_2 = 0.951). The determined crystal-field splitting is different from that in monoclinic Yb:KY$(WO_4)_2$ for which $^2F_{7/2}$ = (0, 169, 407, 568) cm^{-1} and $^2F_{5/2}$ = (10187, 10476, 10695) cm^{-1} [16]. In particular, the total Stark splitting of the ground-state, $\Delta E(^2F_{7/2})$, is larger for Yb:KY$(MoO_4)_2$ (601 cm^{-1}), which explains the broadband emission properties of this material.

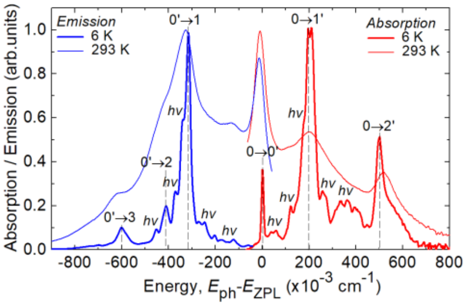

Fig. 8. Absorption and luminescence spectra of Yb^{3+}:KY$(MoO_4)_2$ plotted *vs*. the energy difference ($E_{ph} - E_{ZPL}$), where $E_{ph} = h(c/\lambda)$ is the photon energy and E_{ZPL} = 10246 cm^{-1} is the zero-phonon line (ZPL) energy, measured at LT (6 K) and RT (293 K) with unpolarized light. For LT emission spectra, λ_{exc} = 976 nm. Electronic transitions are indicated as $i \leftrightarrow j'$, phonon sidebands – as $h\nu$.

Previously, for the isostructural KYb(MoO_4)$_2$, it was pointed out that even at LT, the spectra of the Yb^{3+} ion revealed a strong electron-phonon coupling [31]. Thus, the assignment of the Stark levels was complicated. The following splitting for the ground-state ($^2F_{7/2}$) was proposed: (0, 240, 460, 460) cm^{-1}. This poorly agrees with our data.

For all RE ions, the barycenter energy of any isolated $^{2S+1}L_J$ $4f^n$ multiplet depends linearly on the barycenter energy of any other isolated multiplet. This relation is expressed by the barycenter plot [37], Fig. 9(b). The determined barycenter energies $<E(^2F_{5/2})>$ and $<E(^2F_{7/2})>$ agree well with the linear fit to this plot, expressed by the equation $E(^2F_{5/2}) = 10166.6 + 0.997\times E(^2F_{7/2})$ cm^{-1}, where E_0 = 10166.6 cm^{-1} denotes the energy of the Yb^{3+} excited-state for a free-ion. This confirms the correctness of the constructed energy-level scheme.

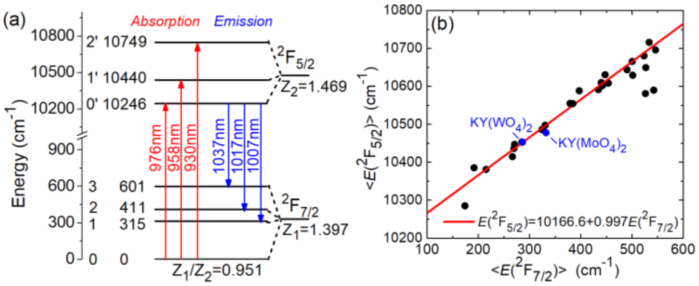

Fig. 9. (a) Crystal-field splitting of the Yb^{3+} ion in the KY(MoO_4)$_2$ crystal (site symmetry: C_2), $Z_{1(2)}$ are the partition functions for the ground- and excited-state, respectively, *arrows* indicate the transitions in absorption / emission at 6 K; (b) barycenter plot [37] for the Yb^{3+} ion showing the position of Yb:KY(WO_4)$_2$ and Yb:KY(MoO_4)$_2$ crystals (*blue circles*).

5. Laser operation

5.1 Laser set-up

The active elements for the laser experiments were fabricated by mechanical cleavage of the 3 at.% bulk Yb:KY(MoO_4)$_2$ crystal along the (100) plane. In this way, we produced a thin cleaved crystal-plate with a thickness t = 286 μm and a high uniformity of ±2 μm over the clear aperture. No post-cleavage treatment (e.g., polishing) was applied to both surfaces which remained uncoated. The crystal orientation corresponded to light propagation along the ***a***-axis (***a***-cut) which is beneficial for the pump absorption providing access to light polarizations $\boldsymbol{E} \parallel \boldsymbol{b}$ and $\boldsymbol{E} \parallel \boldsymbol{c}$ with higher σ_{abs} values, Fig. 6(b).

For laser experiments, we selected a plano-plano (microchip) laser cavity, Fig. 10, formed by a flat pump mirror (PM) coated for high transmission (HT) at ~0.97 μm and for high reflection (HR) at 1.02–1.2 μm, and a set of flat output couplers (OCs) with a transmission at the laser wavelength T_{OC} of 0.5%-10%. Both cavity mirrors were gently pressed towards the crystal-plate resulting in a nearly monolithic design. The geometrical cavity length L_{cav} nearly equaled the crystal-plate thickness t. The whole stack (cavity mirrors and crystal-plate) was passively cooled.

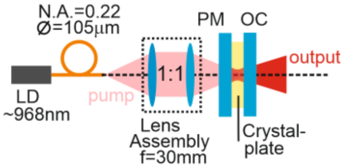

Fig. 10. Scheme of the diode-pumped 3 at.% Yb:KY(MoO_4)$_2$ cleaved crystal-plate microchip laser: LD – laser diode, PM – pump mirror, OC – output coupler.

As a pump source, we employed an InGaAs fiber coupled laser diode (fiber core diameter: 105 μm; numerical aperture (N.A.): 0.22) emitting unpolarized output at a central wavelength of ~968 nm. The pump was collimated and focused into the crystal through the PM using a lens assembly (reimaging ratio: 1:1, focal length: f = 30 mm). The pump spot diameter $2w_P$ in the focus was 100±10 μm. The crystal-plate was pumped in a double-pass, as all the used OCs provided reflection at the pump wavelength, $R \approx 90\%$. The total pump absorption in two passes was estimated from the small-signal value accounting for the Fresnel losses at the uncoated crystal surfaces and amounted to 9.4%. In one pass, $\eta_{abs,0} = 1 - \exp(-\langle\sigma_{abs}\rangle N_{Yb}t) = 4.8\%$, where $\langle\sigma_{abs}\rangle = 0.75\times10^{-20}$ cm^2 is the polarization-averaged absorption cross-section. This value does not account for the ground-state bleaching but at the same time it does not overestimate the laser slope efficiency. Due to the small leakage of the residual pump through the OC, it was difficult to estimate the pump absorption under lasing conditions.

A long-pass filter (FEL1000, Thorlabs) separated the laser output and the residual pump. The laser emission spectra were measured with an accuracy of ±0.2 nm.

5.2 Laser performance

Laser operation was achieved for all the employed OCs. The CW input-output dependences of the diode-pumped microchip cleaved crystal-plate Yb:KY(MoO$_4$)$_2$ laser are shown in Fig. 11(a). For the 1% OC, the laser generated a maximum output power of 0.81 W at 1021-1044 nm with a high slope efficiency (η) of 76.4% *vs*. the absorbed pump power P_{abs}. The laser threshold P_{th} was as low as 56 mW whilst the optical-to-optical efficiency (*vs*. the pump power incident on the crystal) η_{opt} was rather low, 7.0%, owing to the low pump absorption in the thin crystal. With increasing the output coupling, the laser threshold gradually increased, from 55 mW for $T_{OC} = 0.5\%$ to 143 mW for $T_{OC} = 10\%$. The input-output dependences were linear for all the OCs. The absorbed pump power in the crystal-plate P_{abs} was limited to below 1.1 W in order to avoid thermal fracture of the passively cooled crystal.

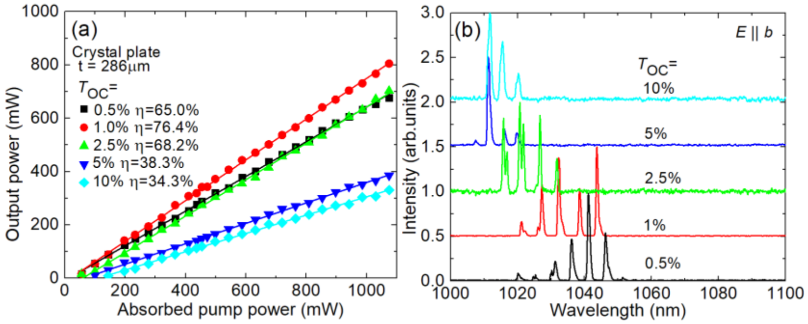

Fig. 11. Diode-pumped Yb:KY(MoO$_4$)$_2$ cleaved crystal-plate microchip laser: (a) input-output dependences, η – slope efficiency; (b) typical laser emission spectra measured at $P_{abs} = 1.0$ W. The laser polarization is ***E*** || ***b***.

Typical laser emission spectra are shown in Fig. 11(b). The spectra experienced a blue-shift with the increase of the output coupling: from 1020-1051 nm for $T_{OC} = 0.5\%$ to 1012-1020 nm for $T_{OC} = 10\%$. This is due to the quasi-three level nature of the Yb^{3+} laser transition $^2F_{5/2} \rightarrow {}^2F_{7/2}$ exhibiting reabsorption. The observed spectral behavior agrees with the gain spectra for ***E*** || ***b***, Fig. 7(b). The laser output was linearly polarized (***E*** || ***b***) naturally selected by the anisotropy of the gain.

The laser spectra were modulated by etalon (Fabry-Perot) effects showing two wavelength separations, $\Delta\lambda_1 = 1.0\pm0.1$ nm and $\Delta\lambda_2 = 6.2\pm0.5$ nm. The smaller one is attributed to the etalon effect of the crystal itself and the larger one – to the residual small airgap between the crystal and one of the cavity mirrors. The free spectral range (FSR) of the Fabry-Perot etalon with a thickness t and a refractive index n at normal incidence is $\Delta\lambda_{FSR} \approx \lambda^2/(2nt)$ which yields 0.95 nm for the crystal (t = 286 μm and $\langle\lambda\rangle$ = 1030 nm). The thickness of the equivalent airgap is ~90 μm. The roughly 20 nm broad laser spectra originated from the large gain bandwidth of Yb^{3+} in KY(MoO$_4$)$_2$.

The laser operation in the plano-plano cavity indicated a positive thermal lens for ***a***-cut Yb:KY(MoO_4)$_2$. Positive thermal lens was observed also for monoclinic Yb:KY(WO_4)$_2$ crystal [38] and ascribed to the counteraction of negative thermo-optic coefficients d*n*/d*T* [39] and the positive thermal expansion. Negative d*n*/d*T* values were also measured for tetragonal double molybdates [40]. Note that for Yb:KY(MoO_4)$_2$, the largest coefficient of linear thermal expansion (38.3×10^{-6} K^{-1}) is along the ***a***-axis which may explain the positive thermal lens for the present crystal cut.

6. Conclusion

To conclude, we report on the growth, structure refinement by the Rietveld method, polarized room-temperature spectroscopy and crystal-field splitting (at 6 K), and first laser operation of Yb^{3+}-doped potassium yttrium double molybdate, Yb:KY(MoO_4)$_2$. Its layered crystal structure dictates a strong polarization-anisotropy of the transition cross-sections for the Yb^{3+} dopant and a perfect natural cleavage habit along the (100) plane. Mechanically cleaved thin crystal films and plates with a thickness as thin as tens of μm can be directly applied as gain medium for laser operation. We report on a watt-level output from a diode-pumped microchip 3 at.% Yb:KY(MoO_4)$_2$ crystal-plate laser operating with a high slope efficiency (76.4%) almost approaching the Stokes limit. Highly Yb^{3+}-doped KY(MoO_4)$_2$ crystal plates and films (e.g., up to 10 at.%, as obtained in our preliminary growth experiments) are attractive for short-pulse (sub-ns) passively Q-switched microchip lasers, as well as thin-disk lasers.

Funding

Russian Foundation for Basic Research (19-32-90199); Spanish Government (MAT2016-75716-C2-1-R (AEI/FEDER,UE)); Catalan Government (2017 SGR 755), National Natural Science Foundation of China (61975208, 51761135115, 61875199, 61850410533), Deutsche Forschungsgemeinschaft (PE 607/14-1).

Acknowledgments

P. L. thanks Ms. Liza Basyrova for the help with the SEM studies.

Disclosures

The authors declare no conflicts of interest.

References

1. H. Zhu, Y. Chen, Y. Lin, X. Gong, Q. Tan, Z. Luo, and Y. Huang, “Growth, spectral properties, and laser demonstration of Yb^{3+}:$BaGd_2(MoO_4)_4$ cleavage crystal”, J. Appl. Phys. **101**(6), 063109-1-8 (2007).
2. Y. J. Chen, Y. D. Huang, X. Q. Lin, Q. G. Tan, Z. D. Luo, and Y. F. Lin, “Laser emission from unprocessed cleavage microchip,” Appl. Phys. Lett. **86**(2), 021115-1-3 (2005).
3. A. Volokitina, P. Loiko, A. Pavlyuk, S. Slimi, R. M. Solé, E. B. Salem, E. Kifle, J. M. Serres, U. Griebner, V. Petrov, M. Aguiló, F. Díaz, and X. Mateos, "Laser operation of cleaved single-crystal plates and films of Tm:KY(MoO_4)$_2$," Opt. Express **28**(7), 9039-9048 (2020).
4. J. J. Zayhowski, “Microchip lasers,” Opt. Mater. **11**(2-3), 255-267 (1999).
5. J. M. Serres, X. Mateos, P. Loiko, K. Yumashev, N. Kuleshov, V. Petrov, U. Griebner, M. Aguiló, and F. Díaz, "Diode-pumped microchip Tm:KLu(WO_4)$_2$ laser with more than 3 W of output power," Opt. Lett. **39**(14), 4247-4250 (2014).
6. P. Loiko, J. M. Serres, X. Mateos, K. Yumashev, A. Yasukevich, V. Petrov, U. Griebner, M. Aguiló, and F. Díaz, "Sub-nanosecond Yb:KLu(WO_4)$_2$ microchip laser," Opt. Lett. **41**(11), 2620-2623 (2016).
7. Y. Chen, X. Gong, Y. Lin, Q. Tan, Z. Luo, and Y. Huang, "Continuous-wave laser characteristics of a Nd^{3+}:LaB_3O_6 cleavage microchip and the influence of thermal effects," Appl. Opt. **45**(32), 8338-8345 (2006).
8. J. Liu, W. Han, X. Chen, D. Zhong, B. Teng, C. Wang, and Y. Li, "Spectroscopic properties and continuous-wave laser operation of Yb:$LuPO_4$ crystal," Opt. Lett. **39**(20), 5881-5884 (2014).
9. X. Zhang, J. He, T. Tang, B. Teng, D. Zhong, X. Xu, and Z. Wang, "Efficient laser operations of unprocessed thin plate of Nd:YPO_4 crystal," Opt. Express **26**(20), 26179-26187 (2018).
10. Y. J. Chen, Y. F. Lin, X. H. Gong, H. M. Zhu, Z. D. Luo, and Y. D. Huang, “805-nm diode-pumped continuous-wave 2-μm laser performance of Tm^{3+}:$BaGd_2(MoO_4)_4$ cleavage plate,” Appl. Phys. B **98**(1), 55-60 (2010).

11. W. Zhao, Y. S. Huang, Z. B. Lin, B. Wei, F. W. Wang, M. Xu, X. Zhao, Q. H. Zheng, and W. W. Zhou, “Spectra and energy levels of a layered Yb^{3+}:$CsGd(MoO_4)_2$ crystal with perfect cleavage: a candidate for microchip lasers, RSC Adv. **5**(44), 34730-34736 (2015).
12. J. Liu, V. Petrov, H. Zhang, and J. Wang, “Power scaling of a continuous-wave and passively Q-switched Yb:$KLu(WO_4)_2$ laser end-pumped by a high-power diode,” Appl. Phys. B **88**(4), 527-530 (2007).
13. P. Loiko, J. M. Serres, X. Mateos, X. Xu, J. Xu, V. Jambunathan, P. Navratil, A. Lucianetti, T. Mocek, X. Zhang, U. Griebner, V. Petrov, M. Aguiló, F. Díaz, and A. Major, "Microchip Yb:$CaLnAlO_4$ lasers with up to 91% slope efficiency," Opt. Lett. **42**(13), 2431-2434 (2017).
14. H. Zhu, Y. Chen, Y. Lin, X. Gong, Z. Luo, and Y. Huang, "Polarized spectral properties and laser demonstration of Nd^{3+}:$BaGd_2(MoO_4)_4$ cleavage crystal," J. Opt. Soc. Am. B **24**(10), 2659-2665 (2007).
15. V. Petrov, M. C. Pujol, X. Mateos, O. Silvestre, S. Rivier, M. Aguiló, R. M. Solé, J. Liu, U. Griebner, and F. Díaz, “Growth and properties of $KLu(WO_4)_2$, and novel ytterbium and thulium lasers based on this monoclinic crystalline host,” Laser & Photon. Rev. **1**(2), 179–212 (2007).
16. A. A. Lagatsky, N. V. Kuleshov, and V. P. Mikhailov, “Diode-pumped CW lasing of Yb:KYW and Yb:KGW,” Opt. Commun. **165**(1-3), 71-75 (1999).
17. J. M. Serres, P. Loiko, X.Mateos, K. Yumashev, N. Kuleshov, V. Petrov, U. Griebner, M. Aguiló, and F. Díaz, "Prospects of monoclinic Yb:$KLu(WO_4)_2$ crystal for multi-watt microchip lasers," Opt. Mater. Express **5**(3), 661-667 (2015).
18. U. Griebner, S. Rivier, V. Petrov, M. Zorn, G. Erbert, M. Weyers, X. Mateos, M. Aguiló, J. Massons, and F. Díaz, “Passively mode-locked Yb:$KLu(WO_4)_2$ oscillators,” Opt. Express **13**(9), 3465–3470 (2005).
19. S. Pekarek, C. Fiebig, M. C. Stumpf, A. E. H. Oehler, K. Paschke, G. Erbert, T. Südmeyer, and U. Keller, “Diode-pumped gigahertz femtosecond Yb:KGW laser with a peak power of 3.9 kW,” Opt. Express **18**(16), 16320-16326 (2010).
20. F. Brunner, T. Südmeyer, E. Innerhofer, F. Morier-Genoud, R. Paschotta, V. E. Kisel, V. G. Shcherbitsky, N. V. Kuleshov, J. Gao, K. Contag, A. Giesen, and U. Keller, "240-fs pulses with 22-W average power from a mode-locked thin-disk Yb:$KY(WO_4)_2$ laser," Opt. Lett. **27**(13), 1162-1164 (2002).
21. S. Rivier, X. Mateos, Ò. Silvestre, V. Petrov, U. Griebner, M. C. Pujol, M. Aguiló, F. Díaz, S. Vernay, and D. Rytz, "Thin-disk Yb:$KLu(WO_4)_2$ laser with single-pass pumping," Opt. Lett. **33**(7), 735-737 (2008).
22. A. Volokitina, P. Loiko, E. Vilejshikova, X. Mateos, E. Dunina, A. Kornienko, N. Kuleshov, and A. Pavlyuk, “Eu^{3+}:$KY(MoO_4)_2$: A novel anisotropic red-emitting material with a layered structure,” J. Alloys Compd. **762**, 786-796 (2018).
23. Y. Chen, Y. Lin, X. Gong, Q. Tan, Z. Luo, and Y. Huang, “Polarized spectral characteristics of Nd^{3+}: $KY(MoO_4)_2$ crystal with perfect cleavage planes: a promising microchip gain medium,” J. Opt. Soc. Am. B **24**(3), 496–503 (2007).
24. P. Loiko, E. Kifle, J. M. Serres, X. Mateos, M. Aguiló, F. Díaz, E. Vilejshikova, N. Kuleshov, and A. Pavlyuk, “Efficient continuous-wave in-band pumped Nd:$KY(MoO_4)_2$ laser,” Laser Phys. Lett. **15**(6), 065002-1-5 (2018).
25. R. F. Klevtsova and S. V. Borisov, “X-ray structural study of the double molybdate $KY(MoO_4)_2$,” Sov. Phys. Dokl. **12**, 1095-???? (1968) [Transl. from Dokl. Akad. Nauk SSSR **177**(6), 1333-1336 (1967)].
26. J. Hanuza and L. Łabuda, “Polarized Raman and infrared spectra of a multilayer $KY(MoO_4)_2$ crystal,” J. Raman Spectrosc. **11**(4), 231-237 (1981).
27. A. A. Kaminskii and S. N. Bagayev, “Ribbon and sheet miniature crystal laser,” Quantum Electron. **24**(12), 1029-1030 (1994).
28. Y. A. Borovlev, N. V. Ivannikova, V. N. Shlegel, Y. V. Vasiliev, and V. A. Gusev, “Progress in growth of large sized BGO crystals by the low-thermal-gradient Czochralski technique,” J. Cryst. Growth **229**(1-4), 305-311 (2001).
29. A. A. Kaminskii, P. V. Klevtsov, and A. A. Pavlyuk, “Stimulated emission from $KY(MoO_4)_2$-Nd^{3+} crystal laser,” Phys. Status Solidi A **1**(3), K91-K94 (1970).
30. R. D. Shannon, “Revised effective ionic radii and systematic studies of interatomic distances in halides and chalcogenides,” Acta Cryst. A **32**(5), 751-767 (1976).
31. G. I. Frolova, L. E. Reznik, and I. E. Paukov, “Crystal-field effects on the thermodynamic properties of the $KLn(MoO_4)_2$ isostructural compounds,” J. Chem. Thermodynam. **21**(1), 25-36 (1989).
32. P. A. Loiko, K. V. Yumashev, N. V. Kuleshov, G. E. Rachkovskaya, and A. A. Pavlyuk, “Detailed characterization of thermal expansion tensor in monoclinic $KRe(WO_4)_2$ (where Re = Gd, Y, Lu, Yb),” Opt. Mater. **34**(1), 23-26 (2011).
33. L. Macalik, J. Hanuza, and A. A. Kaminskii, “Polarized Raman spectra of the oriented $NaY(WO_4)_2$ and $KY(WO_4)_2$ single crystals,” J. Molec. Struct. **55**(1-3), 289-297 (2000).
34. L. A. Kulakova, “Acoustooptical and elastic properties of laminated $KY(MoO_4)_2$ crystals,” Phys. Sol. State **42**(1), 55-58 (2000) [transl. from Fizika Tverdogo Tela **42**(1), 53–56 (2000)].
35. X. Mateos, J. M. Serres, P. Loiko, U. Griebner, V. Petrov, K. Yumashev, M. Aguiló, and F. Díaz, “Indium-modified Yb:$KLu(WO_4)_2$ crystal: Growth, spectroscopy and laser operation,” J. Lumin. **183**, 391-400 (2017).
36. B. Aull and H. Jenssen, “Vibronic interactions in Nd:YAG resulting in nonreciprocity of absorption and stimulated emission cross sections,” IEEE J. Quantum Electron. **18**(5), 925-930 (1982).
37. P. H. Haumesser, R. Gaumé, B. Viana, E. Antic-Fidancev, and D. Vivien, “Spectroscopic and crystal-field analysis of new Yb-doped laser materials,” J. Phys.: Cond. Matter **13**(23), 5427-5447 (2001).

38. P. A. Loiko, S. Manjooran, K. V. Yumashev, and A. Major, “Polarization-anisotropy of thermal lens in Yb:KY(WO_4)$_2$ laser crystal under high-power diode pumping,” Appl. Opt. **56**(10), 2937-2945 (2017).
39. P. A. Loiko, K. V. Yumashev, N. V. Kuleshov, and A. A. Pavlyuk, “Thermo-optical properties of pure and Yb-doped monoclinic KY(WO_4)$_2$ crystals,” Appl. Phys. B **106**(3), 663-668 (2012).
40. P. A. Loiko, X. Han, K. V. Yumashev, N. V. Kuleshov, M. D. Serrano, C. Cascales, and C. Zaldo, “Thermo-optical properties of uniaxial NaT(XO_4)$_2$ laser host crystals, (where T = Y, La, Gd or Bi and X = W or Mo),” Appl. Phys. B. **111**(2), 279-287 (2013).